Electric field measurements in preclinical MRI at 11.7 T and 7 T for experimental SAR comparison

Paul Nobre, Gwenaël Gaborit, Adriano Troia, Umberto Zanovello, Lionel Duvillaret, Olivier Beuf

Electric field measurements in preclinical MRI at 11.7T and 7T for experimental SAR comparison

Paul Nobre[1], Gwenaël Gaborit[2,3], Adriano Troia[4], Umberto Zanovello[4], Lionel Duvillaret[3], Olivier Beuf[1]

[1]Univ. Lyon, INSA-Lyon, Université Lyon 1, CNRS, Inserm, CREATIS, UMR 5220, U1206, 69616 Villeurbanne, France; [2]Université de Savoie, IMEP-LAHC, UMR 5130, 73376 Le Bourget-du-Lac, France; [3]KAPTEOS, 73376 Sainte-Hélène-du-Lac, France; [4]Istituto Nazionale di Ricerca Metrologica, Strada delle Cacce, 91, 10135, Torino, Italy

paul.nobre@creatis.insa-lyon.fr

gwenael.gaborit@univ-smb.fr

a.troia@inrim.it

u.zanovello@inrim.it

lionel.duvillaret@kapteos.com

Corresponding author: Olivier Beuf olivier.beuf@creatis.insa-lyon.fr

Highlights:

• The E-field probe induced no visible alteration of the fields up to 11.7 T.

• The E-field allowed accurate SAR measurement independently of complex heat exchanges

• The Uncertainty of measurement was below 3% for a minimal SAR of 4.10^{-4} W/kg.

• The SAR was 6 times higher at the center of the coil at 11.7 T than at 7 T.

• The repeatability estimated with the coefficient of variation was 2.3%.

Abstract: SAR assessment is a major concern in MRI. The energy absorbed by tissues increases quadratically with the static magnetic field; therefore, ultra-high field (≥7 T) systems require careful dosimetry to exploit their potential. The objectives are to validate the use of electric-field probe for SAR assessment for high-field MRI, and to study the advantages and drawbacks of E-field measurements.

The experiments were performed at 7 and 11.7 T on preclinical systems in a phantom with calibrated dielectric properties. Absolute values of the E-field were measured according to position inside a birdcage coil and electrical conductivity, local temperature increase were simultaneously evaluated with operating RF frequency, as well as the re-positioning precision through five repetitive measurements. Results yielded a 14.8 $\pm$ 0.36 W/kg SAR near the coil's capacitors compared to 8.1 $\pm$ 0.19 W/kg estimated at the center of the coil. The temperature rise was nevertheless higher in the center likely due to heat transfer effects. The SAR measured in similar conditions was 6 times higher at 11.7 T than at 7 T. The probes induced no visible artefact, and the test to estimate the reproducibility of positioning the sensors granted a low 2.3% coefficient of variation. Measuring both the cause (E-field) and the effect (temperature rise) yielded different information, both useful in the context of EM simulation validation.

Keywords: SAR, MR Safety, high magnetic field, E-field sensors, temperature sensors

The authors have no conflict of interest to disclose.

I) Introduction

The main safety concerns regarding MR imaging involve effects due to the high static magnetic fields (projectile effects, active implant dysfunctions), and absorption of radiofrequency (RF) energy by biological tissues[1]. While the former effect has been directly responsible for a few accidents and the death of patients[2], it is considered a manageable risk if strict procedures are followed[3]. The absorption of RF energy however, is inherent to the principle of acquisition and is more complex to approach. The specific absorption rate (SAR) [W/kg] describes the amount of energy transmitted to the body by the RF coil. As such, it is the quantitative value monitored to assure a safe medical examination since high SAR values may cause an excessive temperature increase in tissues[4] and local burns.

The SAR is defined as follows:

$$SAR = \frac{\sigma . E_{rms}^{2}}{\rho} \quad (1)$$

where σ is the electrical conductivity [S/m], E_{rms} is the root mean square of the electric field (E-field) [V/m] associated with the RF magnetic flux density (B1-field) applied for imaging, and ρ is the mass density [kg/m^3]. Faraday's law of induction indicates that the E-field is proportional to the time derivative of the B1-field. Since the time derivative is proportional to the Larmor frequency and to the amplitude of the B1-field, the SAR increases quadratically with the static magnetic field intensity (which is proportional to the Larmor frequency) and with the amplitude of the B1-field (eq.1)[5].

Furthermore, higher frequencies imply a reduced wavelength (λ) of electromagnetic (EM) waves, which in a wide variety of configurations (passive implant, ECG leads, coaxial cables near the patient) is an additional source of hazard[6–8]. For instance, at 11.7 T (as the static field of the new full-body MRI being tested in Paris, or close to the 10.5 T MRI in Minnesota), in a medium with high relative permittivity of 63 such as blood, the half wavelength is about 38 mm. A conductor element of this dimension is sufficient to create a locally strong E-field when submitted to the RF magnetic field[9–11]. It is also worth mentioning that the conductivity of biological tissues increases with frequency[12], and the SAR is proportional to σ as shown in Equation 1.

The growing access to ultra-high field whole body MR scanners (>7 T) is promising for all applications requiring high magnetization[13–16]; however, their compatibility with safety standards needs to be carefully reviewed[17]. The norms and safety standards set the maximum SAR values suggesting possible means to assess it. IEC 60601 states the maximal SAR according to three levels of operating modes, from more to less restrictive. It also depends on the body part (body or head), the type of coil and whether it is global or local (for 10 g of tissue). The SAR limit is usually defined averaged over a 6 minutes period. If we look at the more restrictive mode for the body, the global SAR should not exceed 2 W/kg and 10 W/kg locally.[18]. In order to estimate SAR values, MRI manufacturers rely on numerical simulations, which take into account some morphology factors such as weight or height[19]. Other norms, for

example ASTM F2182 or ISO 10974, address issues of implant carriers and provide guidelines for implant testing.

Whereas the temperature (*T*) increase can be measured as an independent marker, it also allows to retrieve the E-field through Pennes' bioheat equation[20] assuming the knowledge of a few parameters:

$$\rho.C_t.\frac{dT}{dt}=\nabla.k\nabla T+\rho_b.C_b.W.(T_b-T)+Q+\rho.SAR \quad (2)$$

where C_t is the specific heat capacity [$J.kg^{-1}.K^{-1}$], k is the thermal conductivity [$J.s^{-1}.m^{-1}.K^{-1}$], W is the blood perfusion rate [$m^3.s^{-1}.kg^{-1}$], b is the index relative to blood, and Q is the metabolic heat [$J.s^{-1}.kg^{-1}$]. In not perfused media, if the thermal conduction is negligible[21] (e.g. for a short amount of time, before significant heating exchanges), equation (2) can be simplified to:

$$SAR=C_t\frac{dT_t}{dt} \quad (3)$$

While sensors provide absolute and accurate values[22], the fact that they cannot be used non-invasively *in vivo* encourages the comparison between two intrinsically different configurations. If the physical property to be measured has a high spatial dependency, it is possible to fail in determining the maxima, and finally it must also be proven that the sensors do not disturb the measurements. Simulations, on the other hand, allow to represent the human body with the complexity of the tissues - different dielectric parameters, anisotropy, etc. - but make it difficult to estimate the uncertainty of the prediction[23]. The tendency is now to use both simulations and validation measurements in controlled conditions, before using the simulation on complex models[24,25], to provide a safety factor on the output. However, many simulation works still do not correlate the predicted output with measurements, as it involves different disciplines[21]. The difficulties in SAR estimation reside in the complexity of the human body[24], but also in that of the MRI environment and the wide set of parameters impacting the SAR: the proximity to the coil can drastically increase the E-field due to capacitors, and the path of coaxial cables has proven to cause RF burns[26]. To compensate for these constraints, simulations often make use of restrictive criteria, leading to conservative values of SAR[27]. Several other non-invasive MR applications also benefit from validation through E-field and temperature measurements. These include electrical properties tomography (EPT), which provides quantitative information about conductivity and permittivity from the knowledge of the applied B_1-field[28,29] from which the E-field associated with the B_1^+ can be retrieved[30], T1-based thermometry or proton resonance shift thermometry[31,32]. While B_1 mapping techniques could also be used for verification of SAR simulations' output as they have the advantage of being non-invasive, they are sensitive to other effects affecting signal (temperature, field homogeneity, susceptibility) and do not grant the longitudinal component of the E-field[33].

The objective of this study is to validate the use of an E-field sensor for ultra-high field SAR assessment and to quantify its precision and sensitivity. We studied the probe's response with respect to different parameters (position, conductivity media, near a $\frac{\lambda}{2}$ long lead) and compared the measurements of the cause (*i.e.,* E-field) and the associated effect (temperature rise).

II) Materials and methods

a) Materials

Experiments were performed at 7 and 11.7T on a preclinical MRI system (Bruker, Germany). The use of a preclinical system does not limit the validity of the study, as we intend to question the methodology and the benefit/disadvantage of measurements rather than to provide absolute values for a specific configuration. The phantom container consists of a half cylinder with flat bottom (Figure 1). It is 190 mm long and has an inner radius of 32 mm. The phantom container and the sensor holder (Figure 2) were 3D-printed with polylactic acid (PLA). The container was filled with liquid gel composed of water, 21 % (in weight) of polyvinylpyrrolidone (PVP), and 0.25 % of NaCl to set the conductivity[34]. The phantom conductivity was 0.4 S/m with a relative permittivity of 65. Because the phantom is a liquid gel, some non-negligible heat exchanges are expected and the equation 3 is not valid. This is not an issue in our context as our objective is not to match the E-field value with the temperature increase, but to study the validity of E-field measurements in a complex and realistic environments. A Hydroxyethyl Cellulose-based gel could have been used as well, but HEC gels also exhibit strong convective exchange[35], and the PVP gel has the advantage of having its dielectric properties well described according to its concentration[34]. Lastly, it is required to let the solution rest for a few hours for the air bubbles to disappear, which is troublesome when many measurements have to be performed. A RARE 2D MR sequence was repeated without phase encoding gradients. The inner diameter of the RF coils was 72 mm and the length was 100 mm. The details of the sequence parameters and coil architecture used are summarized in Table 1. The center of the phantom container was placed at the RF coil center.

The sensors used are based on optical transmission using optical fibers in order to remove interaction during MR operation. The E-field probe embarks a crystal whose refractive indexes change according to the value of the physical property studied. The modification of the laser beam passing through the crystal allows the measurements. The probes are non-magnetic and non-metallic and are compatible with liquid environments. The E-field sensor is an EoProbe (Kapteos, France) and the temperature sensor is based on another effect, the temperature dependence of the bandgap of a GaAs crystal. It is an OTG-M (OpSens, Canada). Their technical

specifications are given in Table 2. Other studies rely on the E-field to assess SAR in MRI context[36–39]. Most of them make use of metallic dipoles, which are known to alter the field studied, and none of them analyses their performance from a metrology point of view (to our knowledge). In this work we are interested in making use of the probe's linear response to estimate the uncertainty of the protocol, and to compare it to that of a standard temperature measurement. There are a few companies (Healtis, MR:Comp) assessing compatibility of implants who work with such sensors, but the protocol used and the uncertainty of the measurement is usually not available in the literature.

For a sensitivity of 20 mV/(m.Hz$^{1/2}$), the theoretical minimum measurable E-field amplitude is 1 V/m in this context, considering a 2.5-kHz RF pulse bandwidth. This yields a minimum measurable SAR of 4.10^{-4} W/kg (assuming a conductivity of 0.4 S/m and a mass density of 1000 kg/m^3). The uncertainty (u) of the measured E-field is derived from the dynamic of the raw signal (Figure 3), by dividing the voltage of the noise floor by the voltage of the signal. Other sources of errors include the error in the conductivity of the media, evaluated at 2.3% by the authors of the phantom protocol[34]. The uncertainty in SAR is then obtained from the combined standard uncertainties:

$$\frac{u\left(\mathrm{SAR}(E^2,\sigma,\rho)\right)}{\mathrm{SAR}(E^2,\sigma,\rho)} = \sqrt{\frac{4\left(E_x^2 u(E_x)^2 + E_y^2 u\left(E_y\right)^2 + E_z^2 u(E_z)^2\right)}{\left(E_x^2+E_y^2+E_z^2\right)^2} + \frac{u(\sigma)^2}{\sigma^2} + \frac{u(\rho)^2}{\rho^2}} \quad (4)$$

Considering a negligible *u(ρ)*. The uncertainty of every temperature measurement in this study is $\pm$ 0.3 °C with a 99.9% confidence level. The positioning precision of the probes is less than $\pm$ 2.5 mm. The probes are connected to their own processing unit (EoSense or Accusens). Analog signal of the E-field measurement was visualized on a 6-GHz Spectrum analyzer (Keysight, USA) as a power density spectrum in the time domain (150 kHz resolution bandwidth, 500.307 MHz central frequency at 11.7 T). The signal was observed for 12.7 ms to witness at least two full periods of RF pulses. Temperature measurements were recorded on the computer.

b) E-field and temperature measurements

To be suitable for SAR applications, the probes must not alter the EM fields during the MRI acquisition process. This first step was verified by comparing images with and without the sensors. We studied the ability of the probes to detect E-field maxima in the unloaded coil, and to correlate them with the SAR measurement in the worst-case position and at the center of the loaded coil. The E-field in the empty coil was first assessed along the Z-axis by sampling one point per centimeter (purple lines in Figures 1 and 4). The Y position was set by the probe holder, and the X position was chosen to be the closest possible to the coil inner wall to be near the capacitors, because this is a typical worst-case condition encountered in MRI examinations[31]. It

should be noted that there are regions of the phantom closer to the coil walls, but they cannot be reached by the probe holder. At the position of the Z-maxima, the E-field was measured along the X-axis to confirm that it decreases in the center of the coil (blue lines in Figures 1 and 4). After mapping the E-field in the empty coil, the 0.4-S/m phantom was poured into the container and the temperature and E-field were measured at the location corresponding to the worst-case condition (in air), and in the middle of the phantom. The distribution of the E-field can change when modifying the load in the coil, and the worst-case position here refers to the point found in the measurement performed in air. The temperature and the field values were measured simultaneously, in both positions (expected worst-case and RF coil center) using two probes, for a time exposure of 10 min. The E-field and temperature probes were kept as close as possible (Figure 2) using polytetrafluoroethylene (PTFE). The same experiment was also performed at 7 T with a configuration as close as possible as the 11.7 T one (see table 1) to estimate the influence of the operating RF pulse frequency.

We also evaluated the response of the sensors to local effects, such as those encountered at the extremities of metallic implants of the order of half a wavelength[37], and to global variation, such as the impact of the conductivity of the medium. A copper wire was placed inside the phantom, mimicking an elongated conducting non-magnetic implant. Its section was 0.7 mm² and its length was 38 mm (λ/2 at 11.7 T for the considered medium). The wire is aligned with the static magnetic field because it is usually considered the worst case scenario for a straight conductor (no loop)[7], see figure 4. Its extremity, where measurements were performed, was in the center of the coil. The impact of the electrical conductivity on both measurements (*E* and *T*) was also evaluated, by using a second PVP phantom with a higher concentration of NaCl (1.12 %) to reach a conductivity of 1.3 S/m. The impact of the electrical conductivity was tested at 7 T in similar conditions (same sequence and container but different coil). Conductivity values were chosen to be in the typical range of variation encountered in human tissues (cartilage 0.55 S/m - blood 1.32 S/m).

Lastly, the error of positioning and its influence on the SAR assessment were investigated. This was done by repeating five times the same measurement while removing probes and coils between each test. This experiment was carried out at 11.7 T in air to have the highest E-field value. The standard deviation and the coefficient of variation were then established.

c) SAR calculation

To obtain the root mean square of the electric field, we started from the measure of the power density spectrum in the time domain as shown in Figure 3. The signal was triggered on the spectrum analyzer using a standard video trigger level. We isolated one pulse period and calculated the root mean square value of the E-field. The probe was calibrated using a known value of the root mean square E-field. The field was applied in the calibration cell filled with the medium of interest. The ratio between the amplitude of the signal and the actual E-field level is relevant because the probe has

a linear response in the dynamic range given in Table 2. The E-field is a vector, and thus each individual component was measured. *X*- and *Y*-components were obtained with a transverse probe, measuring a component perpendicular to the axis of the probe, and the *Z*-component is obtained with a longitudinal probe. The calibration only has to be performed once, as the optical power of the instrument (Influenced by the temperature or mechanical constrains) is given to the user. To measure the temperature, a long exposure was required (~10 min) in order to witness an increase in temperature of a higher order than the sensitivity of the probe. The specific heat capacity was measured using a calorimeter ($C_c \approx 3450$ J/K).

III) Results

a) E-field mapping

The norm of the E-field along the *Z*-axis can be seen in Figure 5 as a function of *Z* position and time. The *sinc* shape of the pulse with time is recognizable, and the dynamic of the signal is greater than 50 dB. The two local maxima for the E-field magnitude were found near capacitors placed at the extremities of the coil (position 0 and 8). It is worth noting that regarding the longitudinal E-field, a third local maximum was found in the center of the coil but with low transverse components. The position 0 was used as the worst-case reference position for SAR assessment in the rest of the study.

The measurements along the *X*-axis exhibited the expected result, as the field decreased towards the center of the coil. The highest measurement was a 17 kV/m magnitude E-field, to decrease to approximately 12 kV/m in the center of the coil. It is worth noting that the maximal shift from the center on the *X*-axis allowed by the probe holder is 15 mm, but the inner radius of the container is 32 mm, meaning that the worst-case E-field is likely to be higher in this unreachable area.

After placing the phantom inside the container, the SAR at worst-case position was 14.8 W/kg and 8.1 W/kg in the center of the coil. By using the information of the MRI sequence, we can calculate the global power deposit, which is of 3.2 W, and the global SAR which would be 11.4 W/kg. The values measured in the center and on the side of the phantom show that the local SAR varies around the global value, depending on the depth and position. The temperature elevation measured over a time lapse of 10 min was of 3.4 °C and 6.2 °C respectively (Figure 6), meaning that the highest SAR position do not correspond to the highest temperature rise. Both types of probes showed no artifact as depicted on a test image (Figure 7), indicating their compatibility with the 11.7 T field.

b) Local effect, frequency, conductivity, and uncertainty

Measurements made at the tip of the half wave-length wire revealed a SAR equal to 176 W/kg, more than a 20-fold increase from the 8.1 W/kg SAR measured without the wire (E-field pictured in Figure 8). The E-field decreased very rapidly away from the conducting wire, and only a two-fold SAR increase was observed 5 mm away. However, the temperature measurement increased by only 16 % compared to the

situation without the wire. This effect can be hard to observe, and the positioning of the probe can lead to underestimation of temperature increase[40]. The SAR measured in the center of the coil at 7 T was 1.3 W/kg. The energy absorbed in the center of the phantom at 11.7 T was higher as expected, by approximately a factor 6.

The temperature increase was 0.2 °C at 7 T for σ=0.4 S/m and 0.65 °C for σ=1.3 S/m, meaning that the temperature scaled linearly with electrical conductivity, as predicted by theory (this results must be taken with caution as the elevation is close to the sensor's uncertainty). The average E-fields measured were respectively 54.1 V/m and 52.9 V/m, therefore SAR also scaled linearly with the conductivity because of equation 1. The five repeated measurements at the same location gave values of E-field$_{RMS}$ between 448 V/m and 475 V/m with a standard deviation of 10.8 V/m. The coefficient of variation was therefore 2.3 %.

IV) Discussion

While in most cases, the signal dynamic is approximately 50 dB, one low-signal measurement (Y-axis in the center) exhibited a value of 35 dB. We can use this measurement to calculate the percent of error in the E-field (not the calculated SAR). The ratio of the noise voltage (the noise floor visualized on the spectrum analyzer) and the signal voltage yields a $\pm$ 1.7 % uncertainty of measure for the Y-axis, but the other components (X and Z) have both higher values, and lower uncertainties. The error in the sum of the square E-field is $\pm$ 0.8 %. We can add the $\pm$ 2.3 % relative error of the conductivity using equation (4) to reach the final value of $\pm$ 2.4 % of relative error in the SAR. This relative error for a minimum measureable SAR of 4.10^{-4} W/kg allows precise measurements to be made, which is especially relevant in the range of the SAR limits set by the IEC (2 W/kg)[18]. The Uncertainty of the temperature derivative (required for the SAR calculation) is $\pm$ 0.42 °C using Equations (3) and (4), leading to a $\pm$ 2.4 W/kg precision (10 minutes of exposition). Even with a precision of $\pm$ 0.1 °C, as offered by some instruments, the uncertainty is still 0.8 W/kg. A possible way to avoid heat exchange effect is to measure the temperature increase on a short duration before the effect starts to happen, but with a short measure duration, so is the temperature increase, and the elevation can be indistinguishable from the noise level. Regarding the effect of the operating frequency, the reference 22 shows that the SAR augments quadratically only for small object (radius ~20 mm). A 2.8 maximal factor is expected (500^2 MHz/300^2 MHz), because our phantom has a radius relatively small (32 mm). For larger object like the human body, the expected increase would be smaller[22]. If we adjust for the power of the transmit coil (7.42/.4.66, see table 1) it yields a 4.4 times increase which is of the same order of the factor 6 observed. The increase could be due to hardware differences other than the static field. The increase of the conductivity from 300 MHz to 500 MHz could also explain the difference, as the phantom conductivity was calibrated at 300 MHz. While this comparison is difficult to do since transmit RF coils are not strictly identical in geometries (EM coupling is strongly linked to hardware[17]), it is worth noting that every measurement of SAR at 11.7 T confirmed to be significantly higher than at 7 T.

The use of a liquid phantom offered homogeneity and avoided air bubbles, which can be trapped in gels like polyacrylamide acid (PAA) or agar-based medium[39]. The deformability of agar is equally problematic as it is not viscous enough to re-form itself after removing the probe, and the repeatability of an identical measurement is therefore impossible. Air leads to measurements imprecisions, especially for the E-field where the high permittivity gap within the medium of interest is a source of variations. The difference in the measured tendencies between E and T is no surprise, as in a liquid gel (as in the human body), other non-negligible effects occur, such as thermal conduction and convection[41]. The blue curve in Figure 6 exhibits two modes of variation, suggesting thermal regulation. Indeed, the worst position according to SAR is at the extremity of the birdcage, but the SAR decreases rapidly outside the coil (close to the maxima), which creates a situation prone to heat exchange. Additionally the convex temperature trend suggests that the measured points are heating up due to diffusion occurring already from the beginning of the experiment. We inspected this phenomenon and we found that the RF coil itself was heating, and that the close proximity of the phantom was perturbing the thermal equilibrium of the phantom when introducing it in the coil. In this context difficult to predict with simulation, correlating the E-field with the temperature becomes more complex, the simplified equation of Pennes (eq. 3) is inappropriate, and the E-field and temperature give different information.

One of the advantages of preclinical MRI to follow the development of pathologies is to be non-invasive, which is useful in the context of robust statistical methods[42]. For a 40 g mouse, the 3.2 W would yield a 80 W/kg global SAR. We saw in this configuration that moving the probe 20 mm away from the center could double the local SAR. In this context, the absence of SAR limitations in preclinical imaging could be a factor leading to bias in studies (most pathology studies require thermal stability of the animal[43]), as well as burns. Some simulation softwares like Sim4life already propose rodents models, correlating estimations with fast and reliable SAR measurements could rule out this confounding factor in studies where heating could change the biological properties of animals.

Temperature is the criterion that ultimately reflects the safety of an examination for a patient, and it integrates several effects. It requires no additional information to be interpreted, and the variation of conductivity from 0.4 S/m to 1.3 S/m or of frequency is directly reflected in the measured values. The E-field on the other hand, requires knowledge of the dielectric properties to be exploited for SAR estimations, but is the first step in a SAR simulation. For signals with low bandwidth (<MHz), the high dynamic range allows us to detect the E-field in the volt-per-meter range. Its measurement provides information on localized sources, such as the field from the capacitors or the wire tips. Its vectorial nature can be useful to revise a model, and the instantaneous aspect of the measurement has many practical benefits compared to the long exposure time of temperature sensors. Studies have shown that the SAR limit is usually more conservative than temperature limit[44], which is however the harmful effect with damage on cell tissues. Nevertheless, to verify the precision of the temperature computing method, the experimental temperature sensor is still the ground truth and allows to refine and improve the simulation methods.

The main limitations of the study concern the implementation of the measurements: The value of conductivity must be known precisely in order to estimate the SAR. The positioning of the sensors is critical in this kind of application, and hotspots can be missed if a prior numerical model does not guide the measurements. Finally, the E-field and temperature are compared in positions that are as close as possible (<3 mm) but never exactly the same.

Conclusion:

This study demonstrates the relevance of E-field measurements for ultra-high field SAR applications, and shows the advantage of assessing both the E-field and the temperature when evaluating the SAR in a complex environment. The specificities of each physical quantity were outlined: vectorial, instantaneous, and precise even for low values for the E-field; global, easier to calibrate, and assessing the final effect for the temperature. The use of viscous phantoms provided a good permittivity homogeneity.

Acknowledgments

This work was funded by the AURA region and performed within the scope of LabEx PRIMES (ANR-11-LABX-0063). Experiments were performed at the PILoT facility, part of the France Life Imaging infrastructure (ANR-11-INBS-0006).

References

1. Jabehdar Maralani P, Schieda N, Hecht EM, et al. MRI safety and devices: An update and expert consensus. *J Magn Reson Imaging*. 2020;51(3):657-674. doi:10.1002/jmri.26909

2. Hanson LG. Risks related to static magnetic fields. *Physica Medica*. 2016;32:172. doi:10.1016/j.ejmp.2016.07.272

3. Ghadimi-Moghadam A, Mortazavi SMJ, Hosseini-Moghadam A, et al. Does Exposure to Static Magnetic Fields Generated by Magnetic Resonance Imaging Scanners Raise Safety Problems for Personnel? *J Biomed Phys Eng*. 2018;8(3):333-336.

4. Kotze DJ, De Vries C. A quick guide to safety and compatibility of passive implants and devices in an MR environment. *S Afr j radiol*. 2004;8(2):6. doi:10.4102/sajr.v8i2.126

5. Collins CM, Smith MB. Signal-to-noise ratio and absorbed power as functions of main magnetic field strength, and definition of “90°” RF pulse for the head in the birdcage coil. *Magn Reson Med*. 2001;45(4):684-691. doi:10.1002/mrm.1091

6. Kugel H, Bremer C, Püschel M, et al. Hazardous situation in the MR bore: induction in ECG leads causes fire. *Eur Radiol*. 2003;13(4):690-694. doi:10.1007/s00330-003-1841-8

7. Mattei E, Triventi M, Calcagnini G, et al. Complexity of MRI induced heating on metallic leads: Experimental measurements of 374 configurations. *BioMed Eng OnLine*. 2008;7(1):11. doi:10.1186/1475-925X-7-11

8. Zhang B, Wang K, Jiang T. RF power design optimization in MRI system. *Magnetic Resonance Letters*. 2021;1(1):89-98. doi:10.1016/j.mrl.2021.100006

9. Armenean C, Perrin E, Armenean M, Beuf O, Pilleul F, Saint-Jalmes H. RF induced temperature elevation near metallic wires in clinical magnetic resonance imaging. In: *Proceedings of the 25th Annual International Conference of the IEEE Engineering in Medicine and Biology Society, 2003*. Vol 1. ; 2003:501-504 Vol.1. doi:10.1109/IEMBS.2003.1279745

10. Kainz W. MR heating tests of MR critical implants. *J Magn Reson Imaging*. 2007;26(3):450-451. doi:10.1002/jmri.21020

11. Jungmann PM, Agten CA, Pfirrmann CW, Sutter R. Advances in MRI around metal: MRI Around Metal. *J Magn Reson Imaging*. 2017;46(4):972-991. doi:10.1002/jmri.25708

12. Gabriel C, Gabriel S, Corthout E. The dielectric properties of biological tissues: I. Literature survey. *Phys Med Biol*. 1996;41(11):2231-2249. doi:10.1088/0031-9155/41/11/001

13. Ladd ME, Bachert P, Meyerspeer M, et al. Pros and cons of ultra-high-field MRI/MRS for human application. *Progress in Nuclear Magnetic Resonance Spectroscopy*. 2018;109:1-50. doi:10.1016/j.pnmrs.2018.06.001

14. Trattnig S, Springer E, Bogner W, et al. Key clinical benefits of neuroimaging at 7 T. *NeuroImage*. 2018;168:477-489. doi:10.1016/j.neuroimage.2016.11.031

15. Olman CA, Yacoub E. High-field FMRI for human applications: an overview of spatial resolution and signal specificity. *Open Neuroimag J*. 2011;5:74-89. doi:10.2174/1874440001105010074

16. Godlewska BR, Clare S, Cowen PJ, Emir UE. Ultra-High-Field Magnetic Resonance Spectroscopy in Psychiatry. *Front Psychiatry*. 2017;8:123. doi:10.3389/fpsyt.2017.00123

17. Pohmann R, Speck O, Scheffler K. Signal-to-noise ratio and MR tissue parameters in human brain imaging at 3, 7, and 9.4 tesla using current receive coil arrays. *Magn Reson Med*. 2016;75(2):801-809. doi:10.1002/mrm.25677

18. IEC. *Particular Requirements for the Basic Safety and Essential Performance of Magnetic Resonance Equipment for Medical Diagnosis*. https://webstore.iec.ch/preview/info_iec60601-2-33%7Bed3.1%7Db.pdf

19. Stralka JP, Bottomley PA. A prototype RF dosimeter for independent measurement of the average specific absorption rate (SAR) during MRI. *J Magn Reson Imaging*. 2007;26(5):1296-1302. doi:10.1002/jmri.21141

20. Shih TC, Yuan P, Lin WL, Kou HS. Analytical analysis of the Pennes bioheat transfer equation with sinusoidal heat flux condition on skin surface. *Medical Engineering & Physics*. 2007;29(9):946-953. doi:10.1016/j.medengphy.2006.10.008

21. Oh S, Webb AG, Neuberger T, Park B, Collins CM. Experimental and numerical assessment of MRI-induced temperature change and SAR distributions in phantoms and in vivo: Temperature and SAR Distributions in MRI. *Magn Reson Med*. 2010;63(1):218-223. doi:10.1002/mrm.22174

22. Graedel NN, Polimeni JR, Guerin B, Gagoski B, Wald LL. An anatomically realistic temperature phantom for radiofrequency heating measurements: Realistic Temperature Phantom for Radiofrequency Heating Measurements. *Magn Reson Med*. 2015;73(1):442-450. doi:10.1002/mrm.25123

23. Hoult DI. Sensitivity and Power Deposition in a High-Field Imaging Experiment. *J Magn Reson Imaging*. 2000;12(1):46-67. doi:10.1002/1522-2586(200007)12:1<46::AID-JMRI6>3.0.CO;2-D

24. Fiedler TM, Ladd ME, Bitz AK. SAR Simulations & Safety. *NeuroImage*. 2018;168:33-58. doi:10.1016/j.neuroimage.2017.03.035

25. Saniour I, Gaborit G, Perrier AL, et al. Electro-optic probe for real-time assessments of RF electric field produced in an MRI scanner: Feasibility tests at 3 and 4.7 T. *NMR in Biomedicine*. 2018;31(1):e3849. doi:10.1002/nbm.3849

26. Schaller BM, Magill AW, Gruetter R. Common modes and cable traps. :1.

27. Padormo F, Beqiri A, Hajnal JV, Malik SJ. Parallel transmission for ultrahigh-field imaging: Parallel Transmission for Ultrahigh-Field Imaging. *NMR Biomed*. 2016;29(9):1145-1161. doi:10.1002/nbm.3313

28. Xiaotong Zhang et al. - 2014 - Magnetic-Resonance-Based Electrical Properties Tom.pdf.

29. Katscher U, Voigt T, Findeklee C, Vernickel P, Nehrke K, Dossel O. Determination of Electric Conductivity and Local SAR Via B1 Mapping. *IEEE Transactions on Medical Imaging*. 2009;28(9):1365-1374. doi:10.1109/TMI.2009.2015757

30. Martinez JA, Arduino A, Bottauscio O, Zilberti L. Evaluation and Correction of B_{1}^+-Based Brain Subject-Specific SAR Maps Using Electrical Properties Tomography. *IEEE J Electromagn RF Microw Med Biol*. Published online 2023:1-8. doi:10.1109/JERM.2023.3236153

31. Blackwell J, Kraśny MJ, O'Brien A, et al. Proton Resonance Frequency Shift Thermometry: A Review of Modern Clinical Practices. *Magnetic Resonance Imaging*. 2022;55(2):389-403. doi:10.1002/jmri.27446

32. Wang P. Evaluation of MR thermometry with proton resonance frequency method at 7T. *Quant Imaging Med Surg*. 2017;7(2):259-266. doi:10.21037/qims.2017.03.05

33. Xiaotong Zhang, Schmitter S, Van De Moortele P, Jiaen Liu, Bin He. From Complex ${\rm B}_{1}$ Mapping to Local SAR Estimation for Human Brain MR Imaging Using Multi-Channel Transceiver Coil at 7T. *IEEE Trans Med Imaging*. 2013;32(6):1058-1067. doi:10.1109/TMI.2013.2251653

34. Ianniello C, de Zwart JA, Duan Q, et al. Synthesized tissue-equivalent dielectric phantoms using salt and polyvinylpyrrolidone solutions: Synthesized Tissue-Equivalent Dielectric Properties Using a Water-Soluble Polymer. *Magn Reson Med*. 2018;80(1):413-419. doi:10.1002/mrm.27005

35. Liu Y, Hopkins CC, Handler WB, Chronik BA, de Bruyn JR. Rheology and heat transport properties of a hydroxyethyl cellulose-based MRI tissue phantom. *Biomed Phys Eng Express*. 2017;3(4):045008. doi:10.1088/2057-1976/aa7a41

36. Kangarlu A, Tang L, Ibrahim TS. Electric field measurements and computational modeling at ultrahigh-field MRI. *Magnetic Resonance Imaging*. 2007;25(8):1222-1226. doi:10.1016/j.mri.2007.01.115

37. Nordbeck P, Fidler F, Weiss I, et al. Spatial distribution of RF-induced E-fields and implant heating in MRI. *Magn Reson Med*. 2008;60(2):312-319. doi:10.1002/mrm.21475

38. Loader B, Gregory A, Bownds D, Seifert F. Evaluation of an optical electric field sensor for measurement of specific absorption rate (SAR) during magnetic resonance imaging. In: *2012 International Symposium on Electromagnetic*

Compatibility (EMC EUROPE). ; 2012:1-4. doi:10.1109/EMCEurope.2012.6396819

39. Seo Y, Wang ZJ. Measurement and evaluation of specific absorption rate and temperature elevation caused by an artificial hip joint during MRI scanning. *Sci Rep*. 2021;11(1):1134. doi:10.1038/s41598-020-80828-7

40. Mattei E, Triventi M, Calcagnini G, et al. Temperature and SAR measurement errors in the evaluation of metallic linear structures heating during MRI using fluoroptic® probes. *Phys Med Biol*. 2007;52(6):1633-1646. doi:10.1088/0031-9155/52/6/006

41. Yoon KB, Park WH, Kim TK. Estimation of convection heat transfer coefficient and surface emissivity of a nonreacting specimen in cone calorimeter using RPSO method. *J Mech Sci Technol*. 2013;27(6):1575-1580. doi:10.1007/s12206-013-0402-6

42. Seo JH, Ryu Y, Chung JY. Simulation Study of Radio Frequency Safety and the Optimal Size of a Single-Channel Surface Radio Frequency Coil for Mice at 9.4 T Magnetic Resonance Imaging. *Sensors*. 2022;22(11):4274. doi:10.3390/s22114274

43. Denic A, Macura SI, Mishra P, Gamez JD, Rodriguez M, Pirko I. MRI in Rodent Models of Brain Disorders. *Neurotherapeutics*. 2011;8(1):3-18. doi:10.1007/s13311-010-0002-4

44. Boulant N, Wu X, Adriany G, Schmitter S, Uğurbil K, Van De Moortele PF. Direct control of the temperature rise in parallel transmission by means of temperature virtual observation points: Simulations at 10.5 tesla: Control of Temperature Rise in Parallel Transmission. *Magn Reson Med*. 2016;75(1):249-256. doi:10.1002/mrm.25637

Tables

TABLE 1. Sequences and RF coils

Features	11.7 T	7 T
Sequence type	RARE 2D	RARE 2D
RARE factor	128	128
Te, Tr	300 ms, 600 ms	300 ms, 600 ms
Matrix	256 × 128	256 × 128
FOV	64 mm × 32 mm	64 mm × 32 mm
Receive bandwidth	150 kHz	150 kHz
RF pulse bandwidth	2.5 kHz	2.5 kHz
Birdcage type	Bandpass, quadrature	Bandpass, linear
Birdcage legs	16	16
Reference power (amount of power needed for a 90° flip in one ms)	7.42 W	4.66 W
Manufacturer	Bruker	Bruker

TABLE 2. Sensors specifications		
Features	E-field sensor (EoProbe)	Temperature sensor (OTG)
Spatial resolution	5 mm^3	3 mm^3
Temporal resolution	< ns	<1 s
Sensitivity	20 mV/m.$\sqrt{Hz}$	0.05 °C
Uncertainty	Depends on the dynamic	0.3 °C @ 3.3 sigma
Vectorial	yes	no
Dynamic range	130 dB.Hz	0-85°C

Figures

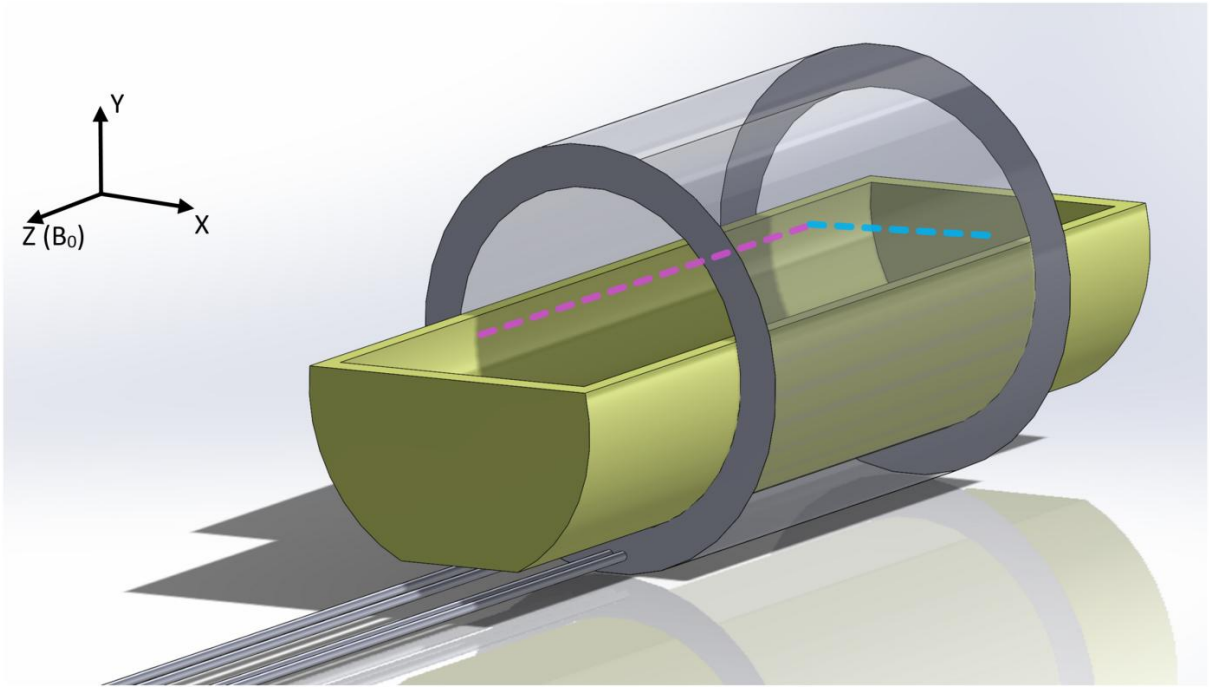

Figure 1: Illustration of the 190 mm-long phantom container in the 100 mm-long RF coil. The dotted lines represent the two axes of measurements in the first experiment to find the SAR hotspots generated by the birdcage.

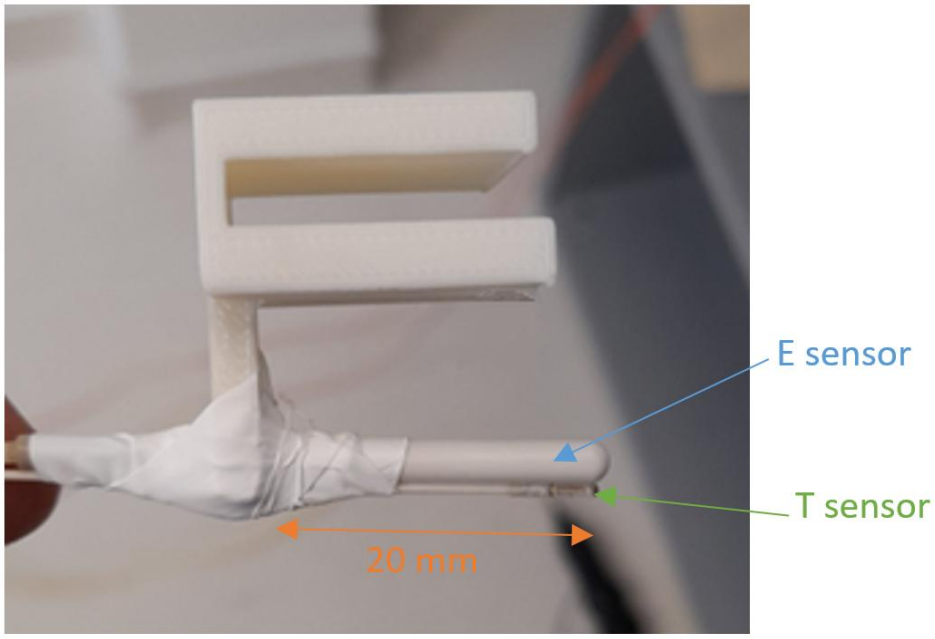

Figure 2: Temperature and E-field probes kept close by and mounted on the moving holder with PTFE. The E-field probe package is 20 mm, but the sensor itself is 5 mm long.

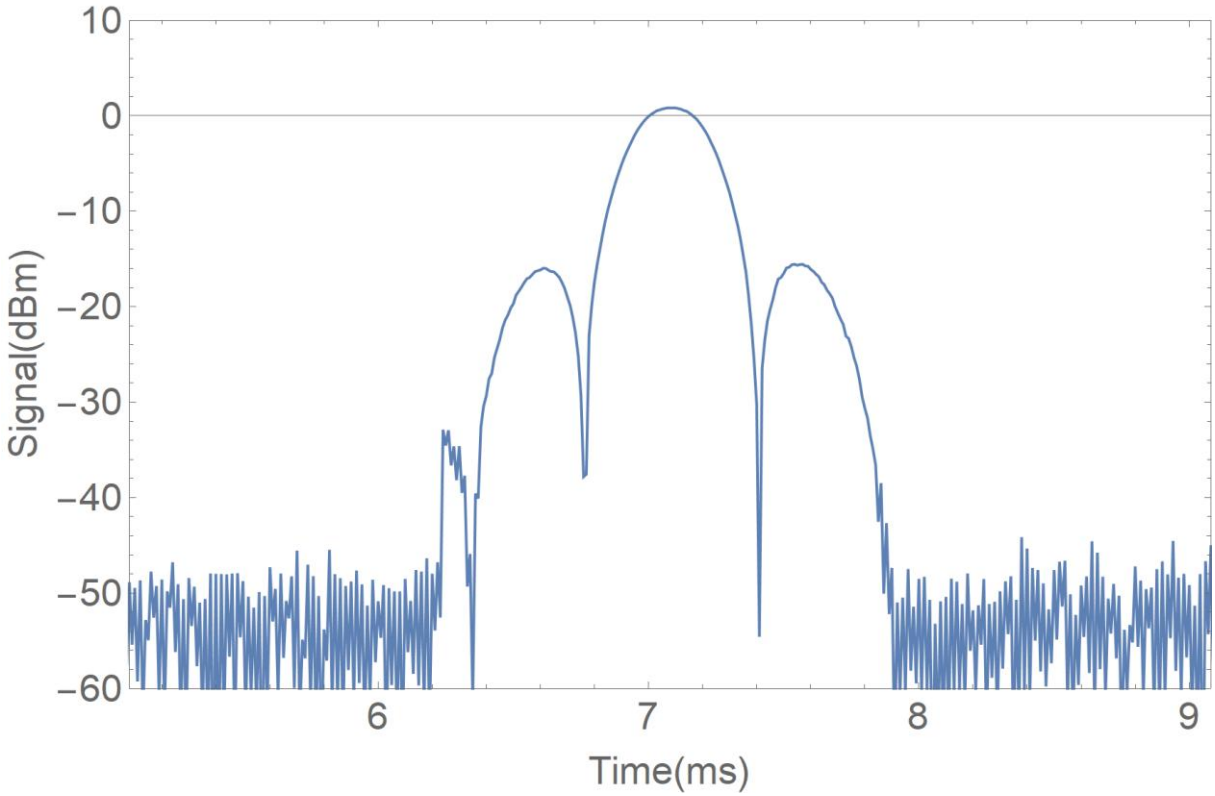

Figure 3: Example of a raw signal visualized in the time domain on the spectrum analyzer. The noise floor is at -50 dBm without averaging, granting more than 50 dB of dynamic range.

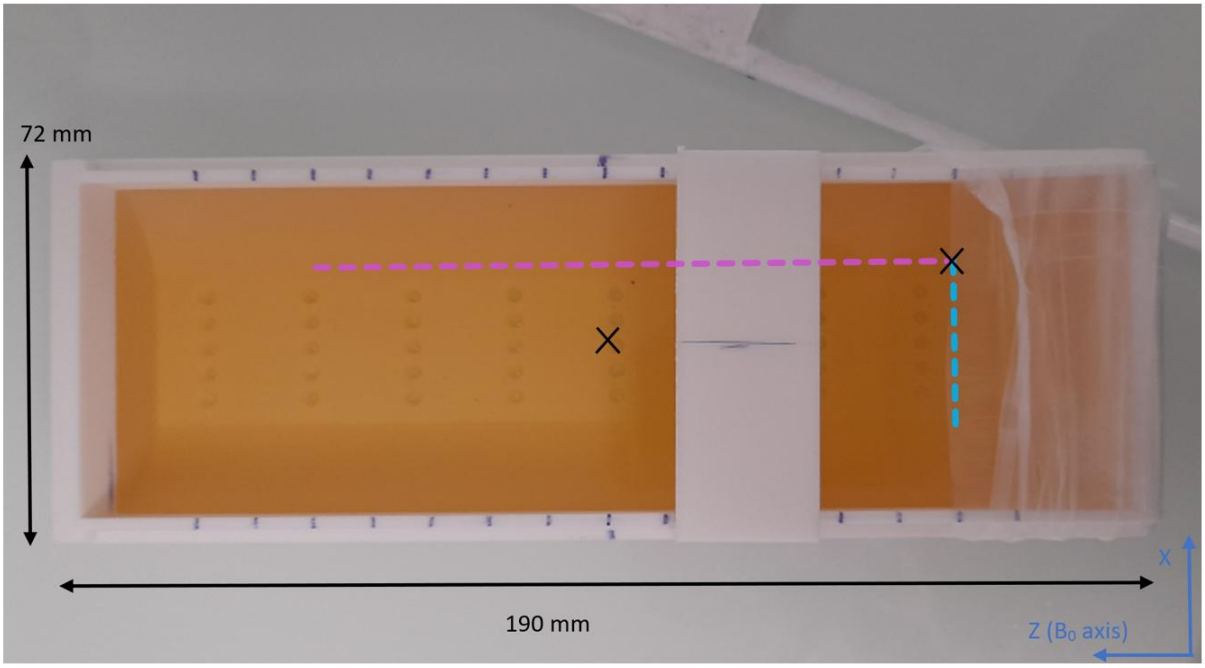

Figure 4: Picture of the 3D-printed container filled with PVP phantom. The white rectangle supported by the edges of the container moves along the Z-axis, and the probe holder mounted beneath it (see Figure 2) moves in the X direction, providing a 2D spatial sampling within the media. The blue line represents the X-axis measurements and the purple line, the Z-axis. The black crosses represent the SAR measurement points.

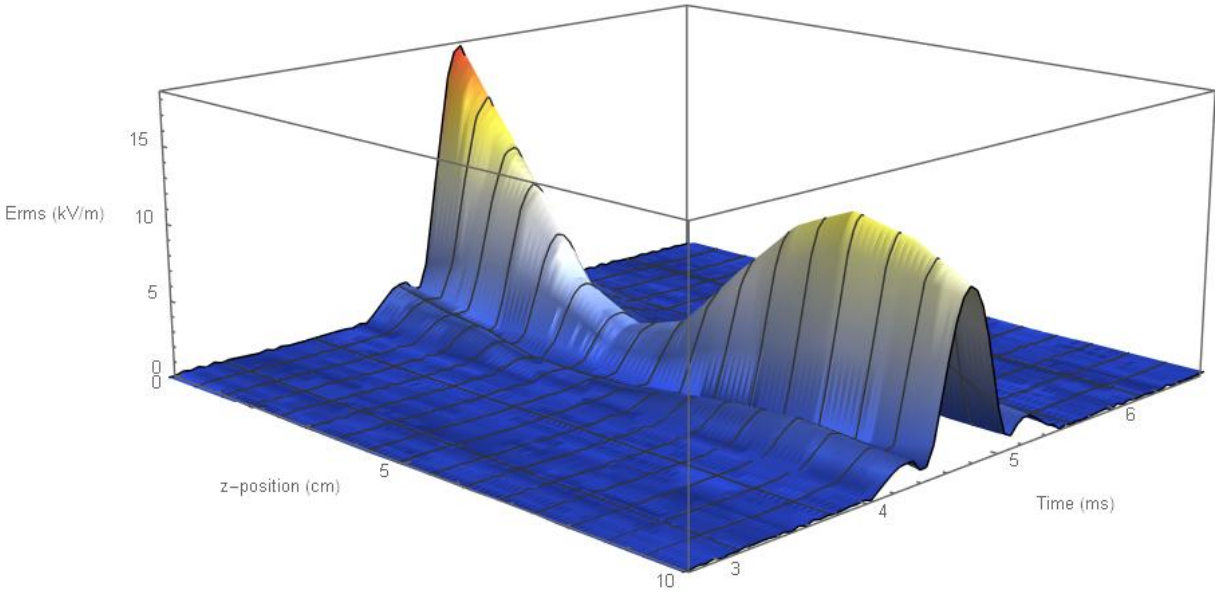

Figure 5: The norm of the RMS electric field according to time and position along the Z-axis. The first maximum is at the entrance of the coil (position 0) and the second one near the other extremity (position 8).

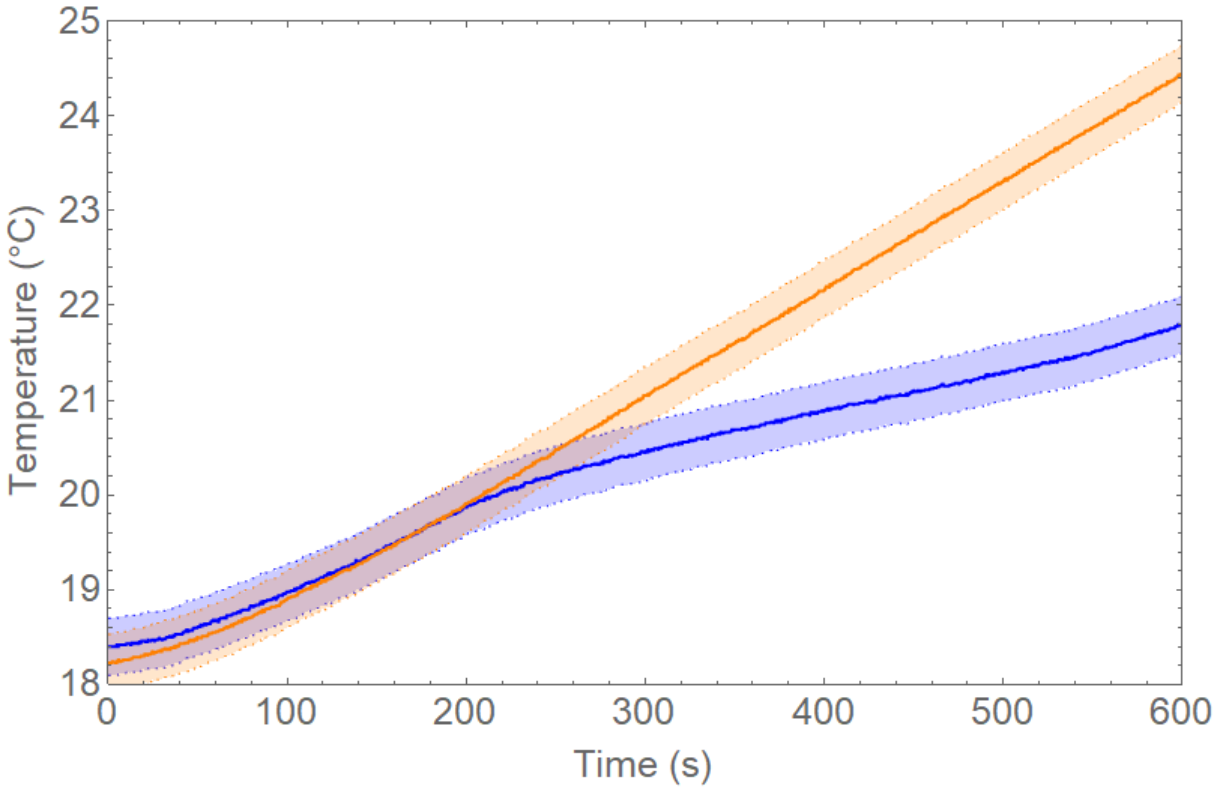

Figure 6: Temporal evolution of the temperature during a 10-min scan measured at the center of the phantom (orange) and leading to the highest SAR (blue). The slope of the orange curve is linear after 100 s, while the blue curves exhibits different slopes, typical of convection effects [41]. The dotted lines represent the uncertainty of measurements.

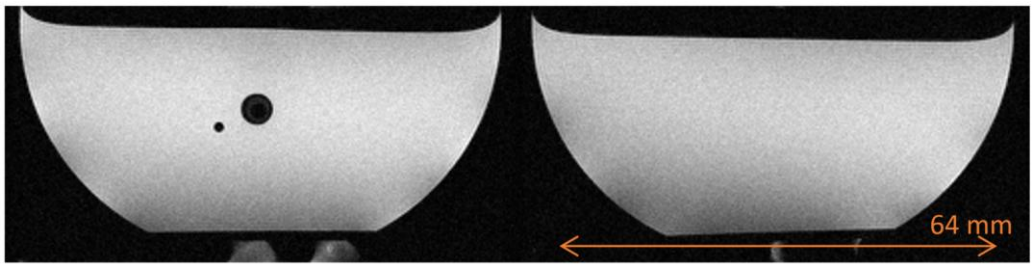

Figure 7: Images acquired with (left) and without (right) the sensors to observe any potential artifacts introduced by the probes. Despite the high static field of 11.7 T, no deterioration is visible. The probes were kept distant on purpose in this configuration.

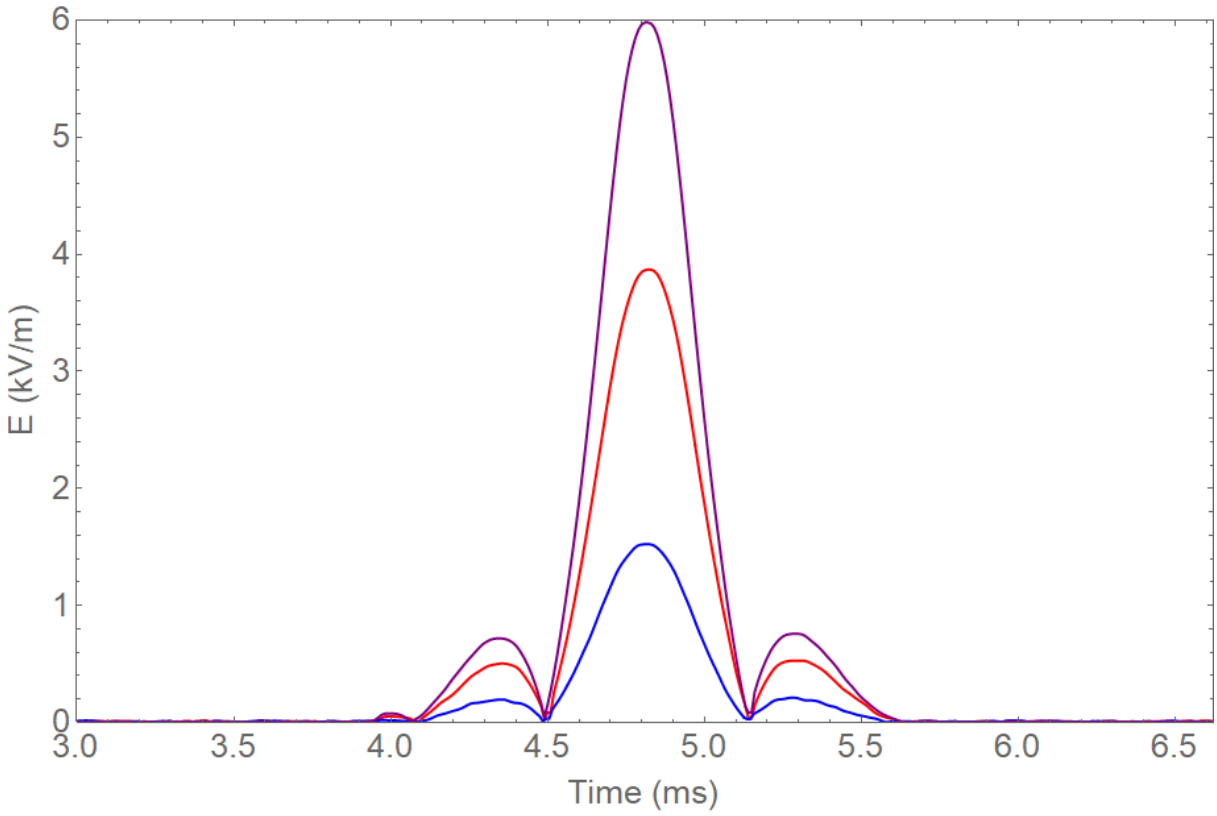

Figure 8: The E-field envelope measured for the three components: X-Y-Z (red, blue, purple) of one of the 128 180° pulses at 11.7 T next to the wire tip. The probe was placed adjacent to the wire on the X-axis (not above or below).